Available online at www.sciencedirect.com

ScienceDirect

ELSEVIER

International Journal of Heat and Fluid Flow 28 (2007) 275–288

International Journal of HEAT AND FLUID FLOW

www.elsevier.com/locate/ijhff

On nonlinear RANS models when predicting more complex geometry room air flows

A. Jouvray, P.G. Tucker *, Y. Liu

Civil and Computational Engineering Centre, School of Engineering, University of Wales Swansea Singleton Park, Swansea SA2 8PP, UK

Received 22 August 2005; received in revised form 10 February 2006; accepted 15 February 2006
Available online 18 May 2006

Abstract

The cubic and explicit algebraic stress (EASM) nonlinear type RANS models are tested for two different room geometries and ventilation regimes. Broadening the works relevance, the flow features found are representative of those observed in low Reynolds number, moderately complex geometry, mixed convection flows in general. The nonlinear models are used with both k–ϵ and k–l base models. The cubic model is also tried in a hybrid LES–RANS strategy. Results are contrasted with linear k–ϵ predictions and LES. Comparison is also made with new velocity, temperature and species concentration measurements. This data is especially designed for the assessment of room ventilation turbulence models. Overall, the EASM shows best RANS model performance. Despite one equation strategies being popular for room ventilation modelling, nonlinear models that use the more complete k–ϵ base model give better results than those using the k–l. As would be expected, the eddy resolving approaches (LES and hybrid LES–RANS) show greatest potential but at extreme computational cost. However, as a result of interfacing issues between the RANS and LES zones, the quality of the hybrid LES–RANS result might be fortuitous. Although the nonlinear models show impressive performance for validation cases on simple geometry flows, for the complex rooms any accuracy gains are case dependent and can be quite minor with high additional computational costs.

Keywords: Room ventilation; RANS; LES; Hybrid LES–RANS

1. Introduction

Room ventilation strategies can essentially be classed as mixed or displacement. With the former, air is both supplied (at relatively high velocity) and extracted at (or around) the ceiling. With this approach the new and older air in the room become relatively well mixed. With displacement ventilation air is supplied at about floor level. This cooler air then rises around hot objects in the room and is extracted at the ceiling. Hence, the study of room ventilation flows has generic relevance to mixed convection, low Reynolds number, moderately complex geometry flows.

Many practical room ventilation design studies make use of zero and one equation turbulence models. As shown by Chen and Xu (1998), these generally provide inferior solutions but at potentially relatively low computational cost. However, for more academic and thorough industrial design studies (see Yoon et al., 2000; Lin et al., 1999; Sinai et al., 2000), the standard linear k–ϵ model is popular. Even so, this model is known to give unsatisfactory predictions for a number of flow configurations. Limitations of the linear k–ϵ model for room ventilation are discussed by Chen (1997). Peng et al. (1996) investigate performances of three two-equations models for prediction of room airflows. It is found that a modified version of the k–ω model (Peng et al., 1997) gives similar predictive accuracy to the k–ϵ but faster iterative convergence.

To increase the predictive accuracy of the standard k–ϵ model, variants such as the Re-Normalisation Group (RNG) of Yakhot et al. (1992), the model of Kim et al. (2001), which includes radiant effects, or the model of Jacobsen and Nielsen (1993) which includes buoyancy effects,

---

* Corresponding author. Tel.: +44 1792 295255; fax: +44 1792 295598.
E-mail address: p.g.tucker@swansea.ac.uk (P.G. Tucker).

0142-727X/$ - see front matter © 2006 Elsevier Inc. All rights reserved.
doi:10.1016/j.ijheatfluidflow.2006.02.029

have been introduced. Variants of the k–ϵ model that have been applied to room ventilation flows are given by Chen (1996).

Jacobsen and Nielsen (1993) investigate the ability of three types of k–ϵ model to predict flows in displacement ventilated rooms. These models (standard k–ϵ, k–ϵ with buoyancy term and the low Reynolds number model of Chikamoto et al., 1992) are compared with temperature and velocity measurements. Despite their differences, all three models are found to give similar overall accuracy levels.

Xu and Chen (2001a) propose a zonal turbulence model for the evaluation of indoor air flows. With this, the one equation model of Rodi et al. (1993) is used in the near wall region ($y^+ < 80$). The standard k–ϵ is used elsewhere. The model is validated for natural and mixed convection cavity flows as well as real room configurations (Xu and Chen, 2001b). It is found to be stable and give encouraging agreement with measurements.

Davidson et al. (2000) show that for certain room flow types linear RANS modelling is inadequate. Then much improved results can be gained with LES (see Davidson and Nielsen, 1996; Peng and Davidson, 2000; Nielsen et al., 1978; Müller and Davidson, 2000). With LES, the large scales are resolved and the small scale eddies are modelled by a Subgrid–Scale (SGS) model. Hence, LES predictions are less model dependent. The simplest and first SGS model to be developed is that of Smagorinsky (1963). This has been applied to room ventilation problems by Emmerich and McGrattan (1998).

Although LES is promising, it is computationally expensive. Hence, this is why here we propose to explore the use of advanced nonlinear RANS models. The cubic model of Craft et al. (1996) and explicit algebraic stress model (EASM) of Gatski and Speziale (1993) are considered in both low Reynolds number k–ϵ and k–l forms. For comparative purposes linear low Reynolds number k–ϵ model simulations are made along with one Smagorinsky LES simulation. In a preliminary way following Batten et al. (2002) the cubic nonlinear model is used to create an LES type model which is suitable for coarser grid simulations.

Comparison is made with measurements for two rooms. The first is the data of Yuan et al. (1999) for a displacement ventilated room. A schematic of this is given in Fig. 1. Secondly, comparison is made with the new data of Jouvray (2003) for both the mixed and displacement ventilation modes. A schematic of the room geometry for this data is given in Fig. 2. With complex room geometries, problem definition (defining complex objects, flow inlet and outlet devices and thermal boundary conditions, etc.) errors can outweigh turbulence model errors. This makes turbulence model assessment especially difficult. The measurements of Jouvray (2003) have been carefully conducted with turbulence model assessment in mind. Hence, boundary conditions have been carefully recorded and problem definition uncertainties kept to a minimum. It is often found that studies of ventilated rooms focus on exploring global air quality parameters rather than the underlying fluid flow structures. For example, Shaw (2000) uses the decay of a contaminant source to evaluate the effects of a range of parameters on ventilation efficiency. The performances of models when predicting global contaminant transport/decay related parameters is also considered here.

2. Turbulence modelling and numerical methods

2.1. Turbulence modelling

The RANS, LES and hybrid RANS/LES models used in this study are briefly described below. The RANS models are the linear k–ϵ (Launder and Spalding, 1974), linear k–l (Wolfshtein, 1969), EASM and cubic. The latter two are formulated using both low Reynolds number k–ϵ and k–l base models. The EASM and cubic eddy-viscosity models have been developed to describe the flow in a more physically consistent manner. The EASM is a computationally inexpensive simplified alternative to the Reynolds Stress Model. Using the EASM, the Reynolds stress tensor is defined as

$$\tau_{ij} = -\frac{2}{3}\rho k\delta_{ij} + 2\mu_{t_1}S_{ij} + 2\mu_{t_2}\frac{k}{\epsilon}(S_{ik}W_{kj} + S_{jk}W_{ki}) - 4\mu_{t_3}\frac{k}{\epsilon}\left(S_{ik}S_{kj} - \frac{1}{3}S_{mn}S_{mn}\delta_{ij}\right), \tag{1}$$

where S_{ij} and W_{ij} are the strain and vorticity rates. The turbulent viscosity μ_{t_i} is evaluated as $\mu_{t_i} = \rho C_{\mu_i}k^2/\epsilon$. Recent trends in turbulence modelling seem to account for the fact that C_μ (=0.09 for the linear k–ϵ model) is not a constant and depends on the flow itself. Here it is defined in a tensor form as

$$C_{\mu 1} = \alpha_1\left[\frac{3(1+\eta^2)}{3+\eta^2+6\zeta^2\eta^2+6\zeta^2}\right], \quad C_{\mu 2,3} = \alpha_1\alpha_{2,3}\left[\frac{3(1+\eta^2)}{3+\eta^2+6\zeta^2\eta^2+6\zeta^2}\right], \tag{2}$$

where η and ζ are known as the invariance coefficients and defined as

$$\eta = \frac{1}{2}\frac{\alpha_3}{\alpha_1}\frac{k}{\epsilon}(S_{ij}S_{ij})^{\frac{1}{2}}, \quad \zeta = \frac{\alpha_2}{\alpha_1}\frac{k}{\epsilon}(W_{ij}W_{ij})^{\frac{1}{2}}. \tag{3}$$

The coefficients α_i are expressed as

$$\alpha_1 = 0.5\left(\tfrac{4}{3} - C_1\right)g, \quad \alpha_2 = 0.5(2 - C_2)g, \quad \alpha_3 = 0.5(2 - C_3)g. \tag{4}$$

The following constants are used: $g = 0.233$, $C_1 = 0.36$, $C_2 = 0.4$, $C_3 = 1.25$ and $C_4 = 6.8$. As noted earlier, use of this model with k–l (Wolfshtein, 1969) and k–ϵ base models is explored. With k–ϵ the Abe et al. (1996) damping functions are used.

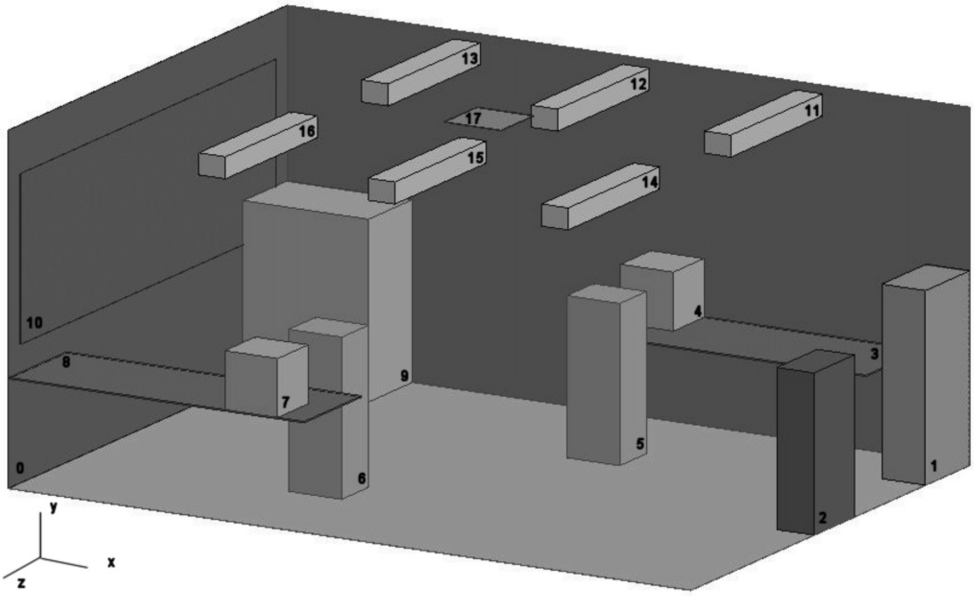

Fig. 1. Room layout for Yuan et al. data set (see Table 1 for a description of items).

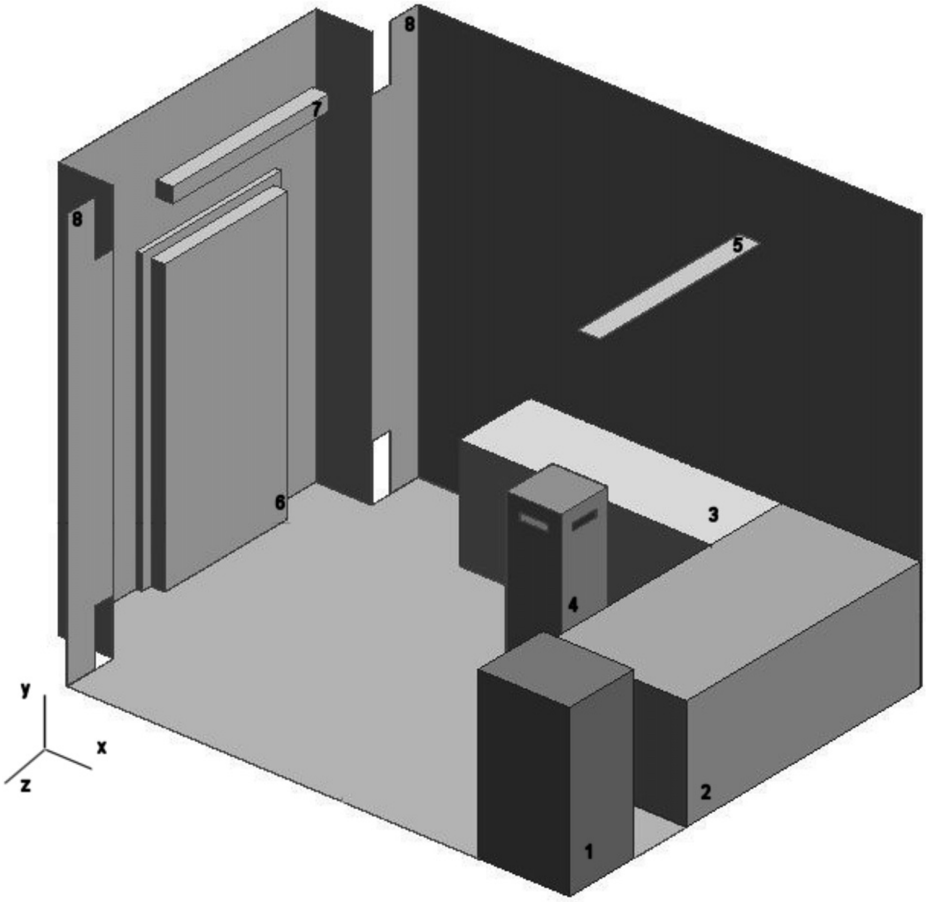

Fig. 2. Room layout for Jouvray data set: (1) filing cabinet, (2) large desk, (3) desk, (4) DIN man, (5) outlet, (6) door, (7) light, and (8) mixed ventilation inlet.

The Craft et al. (1996) cubic eddy-viscosity model is also tested. The use of cubic terms has the distinct advantage over linear and quadratic terms for capturing streamline curvature. The Reynolds stress is calculated by

$$
\begin{aligned}
\tau_{ij} = {} & -\frac{2}{3}\rho\delta_{ij} + 2\mu_t S_{ij} - 4C_1\frac{\mu_t k}{\tilde{\epsilon}}\left(S_{ij}S_{kj} - \frac{1}{3}S_{mn}S_{mn}\delta_{ij}\right) \\
& - 4C_2\frac{\mu_t k}{\tilde{\epsilon}}(W_{ik}S_{kj} + W_{jk}S_{ki}) - 4C_3 \\
& \times \frac{\mu_t k}{\tilde{\epsilon}}\left(W_{ik}W_{jk} - \frac{1}{3}W_{mn}W_{mn}\delta_{ij}\right) - 8C_4\frac{\mu_t k^2}{\tilde{\epsilon}^2} \\
& \times (S_{ki}W_{lj} + S_{kj}W_{li})S_{kl} - 8C_5 \\
& \times \frac{\mu_t k^2}{\tilde{\epsilon}^2}\left(W_{il}W_{lm}S_{mj} + S_{il}W_{lm}W_{mj} - \frac{2}{3}[S_{lm}W_{mn}W_{nl}\delta_{ij}]\right) \\
& - 8C_6\frac{\mu_t k^2}{\tilde{\epsilon}^2}(S_{ij}S_{mn}S_{mn}) - 8C_7\frac{\mu_t k^2}{\tilde{\epsilon}^2}(W_{ij}W_{mn}W_{mn}).
\end{aligned}
\tag{5}
$$

The coefficients C_i have been evaluated using empirical calibrations based on various shear flow configurations. They are defined as: $C_1 = -0.1$, $C_2 = 0.1$, $C_3 = 0.26$, $C_4 = -1.0$, $C_5 = 0.0$, $C_6 = -0.1$ and $C_7 = 0.1$. The turbulent viscosity μ_t is evaluated using the standard k–ϵ ($\mu_t = \rho C_\mu f_\mu k^2/\epsilon$) or appropriate k–l ($\mu_t = \rho C_\mu l_\mu k^{1/2}$) expressions. Here again, C_μ is introduced as the following flow dependent variable:

$$C_\mu = \frac{0.3}{1 + 0.35[\max(S^*, W^*)]^{\frac{3}{2}}}\left[1 - \mathrm{e}^{-0.36\mathrm{e}^{0.75\max(S^*,W^*)}}\right], \tag{6}$$

where S^* and W^* are dimensionless strain and vorticity rates.

In LES a separation of eddy scales is assumed. The larger are resolved whereas the smaller eddies (universal in nature) are modelled by the SGS Stress. For comparative purposes a Smagorinsky LES simulation is made. The SGS tensor τ_{ij} is expressed as

$$\tau_{ij} = \widetilde{u_i u_j} - \tilde{u}_i\tilde{u}_j = \frac{\tau_{kk}}{3}\delta_{ij} - 2\mu_{\mathrm{sgs}}S_{ij}, \tag{7}$$

where μ_{sgs} is the SGS eddy viscosity. For the Smagorinsky model, μ_{sgs} is computed by

$$\mu_{\mathrm{sgs}} = \rho l_{\mathrm{sgs}}^2|\overline{S}|, \tag{8}$$

where l_{sgs} is the modelled length scale, and $|\overline{S}| = \sqrt{2S_{ij}S_{ij}}$ is the magnitude of the strain rate tensor based on the resolved velocities. The scale l_{sgs} is obtained from

$$l_{\mathrm{sgs}} = \min(C_{\mathrm{s}}\Delta, \kappa y_{\min}), \tag{9}$$

where C_{s} is the Smagorinsky constant, $\kappa = 0.42$ is the von Karman constant and $y_{\min}$ the normal distance to the nearest wall. In this study, the volume based 'filter' width $\Delta = (\Delta x\Delta y\Delta z)^{1/3}$ is used, where Δx, Δy and Δz are grid spacings.

Hybrid RANS-LES models have been developed as a compromise between the high accuracy of the LES and the low computational expense of RANS models. Hybrid RANS-LES are found under two main categories: zonal models (see Davidson, 2001; Tucker and Davidson, 2004) and embedded models. LNS of Batten et al. (2002) is an embedded hybrid RANS-LES model in which no fixed boundary exists between the RANS and the LES part of the flow. The transition between RANS and LES is achieved by scaling the effect of the turbulent viscosity of the RANS model (see Speziale, 1998). The scaling coefficient used (α) is defined as a function of turbulent length and velocity scales for both the RANS and the LES models. In this study, the LNS model makes use of the cubic (k–ϵ) and the Smagorinsky models. Using these, α is defined as follows:

$$\alpha = \frac{\min\left(C_{\mathrm{s}}(\Delta^2 S_{ij}^*, C_\mu k^2/\epsilon + \Omega)\right)}{C_\mu k^2/\epsilon + \Omega}, \tag{10}$$

where, C_{s} is the Smagorinsky constant (0.05), Δ the grid spacing (taken as $\max(\Delta x, \Delta y, \Delta z)$) and Ω is a small number used to avoid a singularity.

To model buoyancy in the momentum equations the Boussinesq approximation is used. An extra source term G_k that accounts for the production of turbulence by buoyancy forces is also utilized. The modelling of G_k is the subject of numerous studies (i.e., Peng, 1998). Here due to its simplicity, the widely used standard gradient diffusion hypothesis is used. In this approach,

$$G_k = -g\beta\frac{\mu_t}{\rho Pr_t}\frac{\partial T}{\partial y}, \tag{11}$$

where β is a volumetric expansion coefficient. For the k–l and k–ϵ models, the source term G_k is added to the k equation. In the ϵ equation, the production term P_k is re-written to include buoyancy effects as follows:

$$\frac{\epsilon}{k}(P_k + G_k)(1 + C_3R_f), \tag{12}$$

where R_{f} is the Richardson number defined here as

$$R_f = -\frac{G_k}{G_k + P_k}, \tag{13}$$

and $C_3 \simeq 0.8$ (see Rodi, 1975).

2.2. General numerical modelling

The turbulence models have been implemented in the NEAT solver (Tucker, 2001) and validated for a selection of benchmark problems (see Jouvray, 2003) including plane and sharply turned channel flows, the flow over a backwards facing step and secondary motions (Prandtl's motions of the second kind) in a square duct.

NEAT is a well validated finite volume solver that uses a structured staggered grid arrangement (see Patankar and Spalding, 1972). The results presented here use the second-order central difference scheme for both the convection and diffusion terms. For LES and hybrid simulations the Crank–Nicolson time scheme is used. For stability, even steady state solutions are time marched with relatively small time steps. To model movement of a passive scalar a standard convection, diffusion transport equation with a Schmidt number of one in the diffusion term is used. When this equation is solved for concentration decay, a first order backwards difference temporal scheme is used.

For the cubic model the original wall distance based Yap (1987) correction is used. The wall distance (as with the other models used here needing the wall distance) is evaluated from a Poisson equation that gives a smoothly varying distance field (see Tucker, 2001). For the cubic model, the more basic stabilizing measures with respect to discretized equation diagonal dominance outlined in Craft et al. (1999) are used. Also, C_μ is limited so that it has a maximum value of 0.09. The nonlinear terms/formulations are introduced in a staged fashion for the different transport equations and also ultimately (initially a constant is C_μ used) for the C_μ formulation. In previous work, to gain convergence, for both the EASM and cubic models, for other low Reynolds number flows we have resorted to limiting the magnitudes of the nonlinear term contributions through clipping (see Tucker et al., 2003). However, the potentially accuracy reducing approach was not resorted to here.

3. Measurement data details

Comparison is first made with the velocity and temperature measurements of Yuan et al. (1999) (Y1 Data Set) for a displacement ventilated room. Also, comparisons are made with the new data of Jouvray (2003) for both displacement (J1 Data Set) and mixed (J2 Data Set) ventilation modes. With this data, considerable effort has been made to remove problem definition and boundary condition uncertainties.

Fig. 1 gives a schematic of the Y1 room geometry. The Y1 data comprises measurements along nine vertical axes of the room equi-spaced along the x and y axes. The velocities are measured using hot sphere anemometers and have an uncertainty of ±0.01 m/s. The temperature uncertainty is known to be about ±0.3 °C.

The J1 and J2 measurements, for the Fig. 2 geometry, include hot sphere anemometer velocity (accuracy ±0.02 m/s), thermistor velocity (accuracy ±0.025 m/s), thermistor temperature (accuracy ±1 K) and further anemometer temperature data with an accuracy of ±0.2 K. Wall temperatures are measured using thermocouples with an accuracy of ±0.8 K. The concentration of a passive scalar (SF_6) is also measured. The uncertainty in this scalar data is difficult to quantify. To minimize thermal radiation low emissivity surfaces are used.

Full details of the Fig. 2 room dimensions and elements can be found in Fig. ADM1 of additional material or Jouvray (2003). To save space these details are not reproduced here.

Likewise, precise locations of the 18 hot sphere anemometer based velocity and temperature and 12 thermistor based velocity and temperature measurements (localized to the idealized room occupant) can be found in Fig. ADM2 of additional material or Jouvray (2003). Such information is not necessary to follow the results discussion.

A total of 27 thermocouples have been used to capture the thermal behaviour of the test room's walls (see Fig. ADM3 of additional material or Jouvray (2003) for precise locations). Another three thermocouples have been used to monitor the thermal stratification of the air. These are placed in the middle of the room at dimensionless heights of $Y = 0.25$, 0.5 and 0.6, respectively, where $Y = 1$ is the maximum system extent.

The diffusion of a pollutant source is measured in the Jouvray (2003) data set. To mimic a breathing person, the pollutant/scalar source has been placed in the vicinity of the top of the idealized occupant (DIN man). The location is such that the pollutant itself will be entrained by the thermal plume from the occupant. The scalar concentration is measured at six locations that are mainly in the breathing zone of a typical standing person ($Y = 0.533$). Although it cannot be seen from Fig. 2, at its base, the idealized occupant has rectangular openings at each of its four faces. Full details of the pollutant source and measurement point locations can be found in Fig. ADM4 of additional material or Jouvray (2003).

4. Numerical modelling details

4.1. Yuan et al. (Y1) case

Table 1 summarises the dimensions, locations and convective heat loads for each of the room's components. The radiative heat element has not been considered in this study. Estimates of this and its use to obtain convective components can be found in Jouvray (2003). The flow inlet is on the side of block 2 that faces item 10 (the window). Like most ventilation inlets, a grill is present at the inlet's surface. Hence, only 10% of the inlet area is effective. Since the grill geometry is not resolved here, the inlet velocity is evaluated according to the effective area of the grill. The inlet velocity is ≃0.834 m/s. The outlet is modelled as a plain opening in the ceiling with simple zero gradient

Table 1
Dimensions of the room configuration (dimensions in m)

Label	Description	$x_{\min}$	$x_{\max}$	$y_{\min}$	$y_{\max}$	$z_{\min}$	$z_{\max}$	Q (W)
0	Room	0.0	5.16	0.0	2.43	0.0	3.65	–
1	Cupboard 1	4.83	5.16	0.0	1.32	0.0	0.58	–
2	Inlet	4.88	5.16	0.0	1.14	1.51	2.04	–
3	Table 1	2.50	4.81	0.74	0.75	0.0	0.75	–
4	PC 1	2.78	3.18	0.75	1.14	0.1	0.5	92
5	DIN 1	2.78	3.18	0.0	1.1	0.85	1.20	49
6	DIN 2	1.63	2.03	0.0	1.1	2.45	2.8	49
7	PC 2	1.63	2.03	0.75	1.14	3.15	3.55	174
8	Table 1	0.0	2.23	0.74	0.75	2.90	3.65	–
9	Cupboard 2	0.0	0.95	0.0	1.24	0.0	0.58	–
10	Window	0.0	0.02	0.94	2.1	0.16	3.50	–
11	Light 1	3.93	4.13	2.18	2.33	0.16	1.36	24
12	Light 2	2.63	2.83	2.18	2.33	0.16	1.36	24
13	Light 3	1.35	1.55	2.18	2.33	0.16	1.36	24
14	Light 4	3.93	4.13	2.18	2.33	2.29	3.50	24
15	Light 5	2.63	2.83	2.18	2.33	2.29	3.50	24
16	Light 6	1.35	1.55	2.18	2.33	2.29	3.50	24
17	Outlet	2.35	2.78	2.43	2.43	1.51	2.04	

boundary conditions. The inlet flow temperature is set to 17.2 °C.

Measured surface temperatures are also used as boundary conditions. The data provided does not allow specification of a thermal stratification along each wall. Thus averaged wall temperatures are used. These are as follows: Front wall (maximum z coordinate, i.e., $Z = 1$): 22.65 °C, Back wall: 22.90 °C, East wall (minimum x coordinate): 22.57 °C, West wall: 21.69 °C, Floor: $\simeq$21.87 °C and Ceiling: 22.87 °C. The sensitivity of results to the average wall temperature assumption is discussed later for the Jouvray case. The window is assumed isothermal with a temperature of 27 °C.

A grid of $117 \times 69 \times 83$ (x, y, z) nodes is used for the simulations. Taking into account all solid surfaces, this grid gives an average first off wall $y^+ \simeq 0.9$. It is worth noting that, for this low Reynolds number flow, Yuan et al. find sensibly grid independent solutions for a mesh having over 13 times fewer cells than used here. Also, the convective scheme used by Yuan et al. is more dissipative than that used here.

4.2. Jouvray cases (J1 and J2)

The inlet velocities are set at measured values. These are 0.07386 and 0.3693 m/s for cases J1 and J2, respectively. Similarly inlet airflow temperatures of 297.65 and 294.55 K for cases J1 and J2 are also specified. The outlet, is modelled as a plain opening in the ceiling with simple zero gradient boundary conditions.

4.2.1. Boundary and initial conditions

As with the Y1 case, avoiding modelling uncertainties, measured wall temperatures are used as boundary conditions. For case J1, two types of wall temperature specification are tested. They are:

- Averaged wall temperature and,
- Specification of vertical thermal stratification.

For case J2, only averaged wall temperatures are used. The averaged wall temperatures of cases J1 and J2 are summarised in Table 2.

For the specification of the vertical temperature stratification a quadratic polynomial of the form:

$$T_s(K) = \alpha_t y^2 + \beta_t y + \gamma_t \tag{14}$$

is used where, T_s is the surface temperature and, y is the local height in the room. The coefficients α_t, β_t and γ_t are calculated from a polynomial fit to the measurements and are given, for each wall of case J1, in Table 3. For the floor and ceiling, averaged surface temperatures are used.

Table 2
Averaged wall temperatures for cases J1 and J2

Temperature (K)	Door	Back wall	Left wall	Right wall	Floor	Ceiling
Case J1	297.99	298.09	298.78	297.97	297.37	298.34
Case J2	294.61	295.06	294.91	294.74	294.94	295.11

Table 3
Coefficients of the polynomial fit for wall temperature of case J1

	Left wall	Right wall	Door	Back wall	DIN man J1	DIN man J2
α_t	−0.222	0.008	−0.669	0.142	−0.032	−1.067
β_t	0.950	0.250	2.150	−0.028	1.956	3.539
γ_t	297.40	297.51	296.51	297.65	300.98	297.84

The specification of the idealized occupant heat source is crucial in this study, especially for case J1. A quadratic polynomial fit to the measurements is used to specify, as boundary conditions, the vertical variation of the occupant's surface temperature for both cases. Eq. (14) coefficients describing the idealized occupant's surface temperature can be found in Table 3.

Measured velocities and temperatures at the top and bottom openings of the idealized occupant are also specified as boundary conditions (full details of the locations of thermistor based velocity and temperature probes in the occupant zone can be found in Fig. ADM4 of additional material or Jouvray (2003)). Temperatures and velocities at the top are on average 301.5 K and 0.3 m/s, respectively. At the bottom the averaged velocity is 0.09 m/s. The flow directions at the top and bottom openings of the occupant are assumed surface normal.

When modelling the temporal passive scalar decay, the averaged measured concentration of sampling points located at $Y = 0.533$ (the breathing zone) are used as initial conditions. These are 25.56 and 51.50 ppm, respectively, for cases J1 and J2 and are set at uniformly in the room.

For both cases, a grid of $75 \times 83 \times 63$ (x, y, z) nodes is used. This gives an average first off wall y^+ value of 0.45 for both cases. The near wall LES grid has been modified to ensure cross streamwise non-dimensional grid spacings (Δx^+, Δy^+ or Δz^+) are below 25 wall units (again this figure is based on an average for all solid surfaces). The relatively low Reynolds numbers allow such small values to be obtained.

5. Results and discussion

5.1. Yuan et al. (Y1) case

Fig. 3 shows four velocity profiles (at $X = 0.833$, $Z = 0.5$; $X = 0.5$, $Z = 0.5$; $X = 0.5$, $Z = 0.33$ and $X = 0.5$, $Z = 0.833$) for the linear (Lam and Bremhorst, 1981), EASM (with AKN damping function) and cubic k–ϵ models. The figure indicates that all the models predict magnitudes in line with the experiment with only minor solution differences. Fig. 4 compares the same profiles shown in Fig. 3 but for the k–l based models. The figure shows that the profiles for these models are less monotonic than those for the k–ϵ based models. The lower monotonicity could

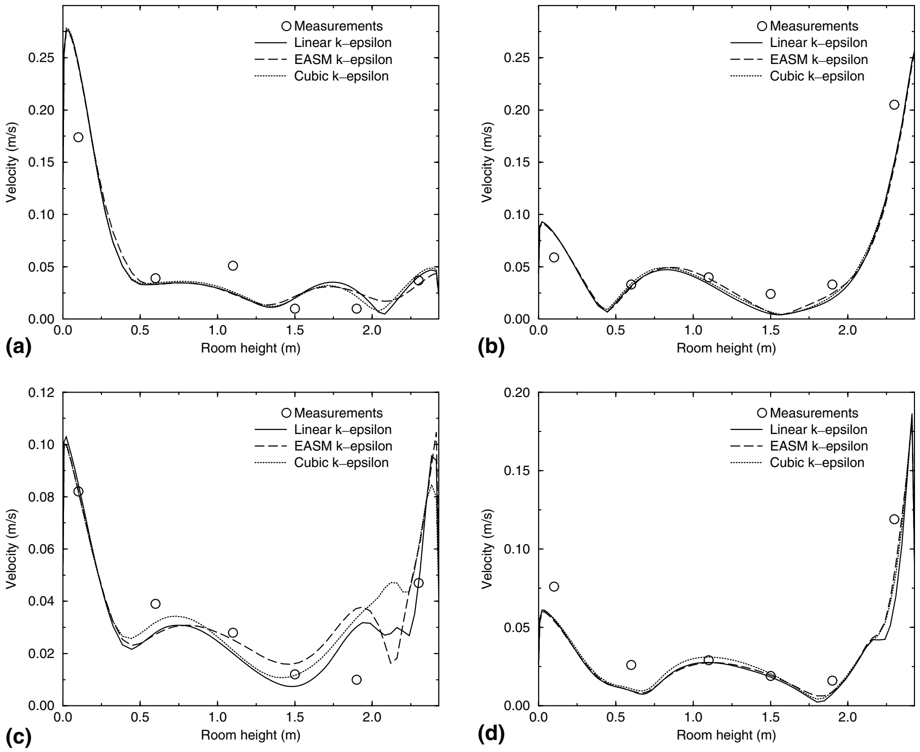

Fig. 3. Comparison of measured velocity profiles with predictions of the linear, EASM and cubic k–ϵ models at the following locations: (a) $X = 0.833$, $Z = 0.5$; (b) $X = 0.5$, $Z = 0.5$; (c) $X = 0.5$, $Z = 0.33$ and (d) $X = 0.5$ and $Z = 0.833$.

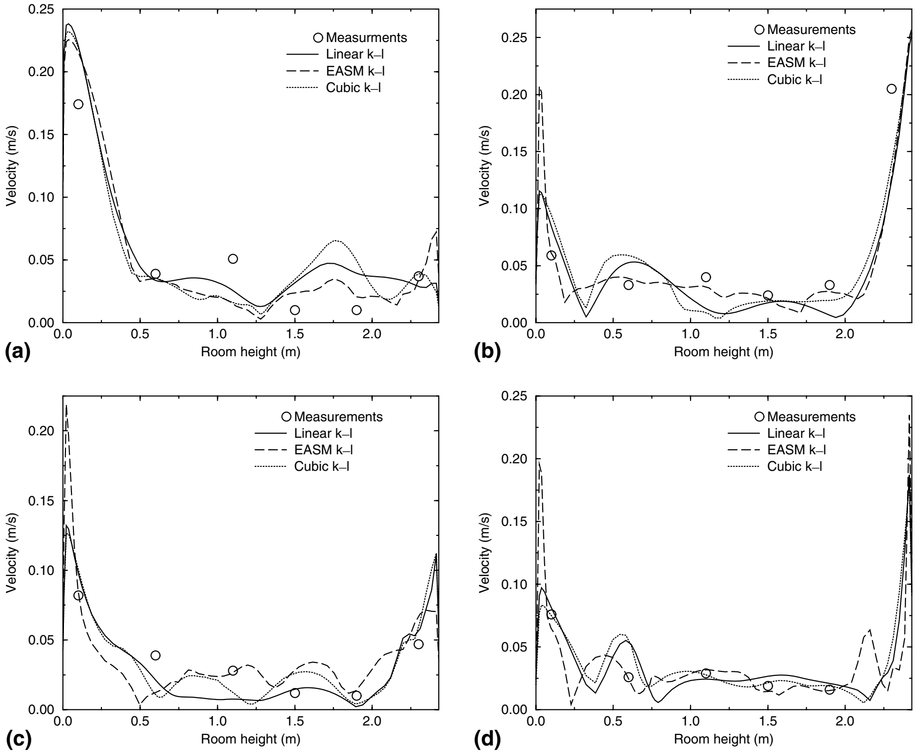

Fig. 4. Comparison of measured velocity profiles with predictions of the linear, EASM and cubic k–l models at the following locations: (a) $X = 0.833$, $Z = 0.5$; (b) $X = 0.5$, $Z = 0.5$; (c) $X = 0.5$, $Z = 0.33$ and (d) $X = 0.5$ and $Z = 0.833$.

partly be attributed to the less smooth turbulence dissipation scale, which is to a greater extent a function of surface locality. With systems cluttered with relatively block like geometries the latter changes rapidly. Fig. 4 also shows that the differences between the linear, EASM and cubic models are greater when used in a k–l framework. Presumably, this is as a consequence of the less monotonic turbulence length scale distribution becoming magnified, in different ways, by the extra nonlinear terms.

The differences observed between the linear k–ϵ and EASM models are also illustrated in a qualitative sense in the Fig. 5 the velocity contour plot. The contours are taken in the x–y plane at $Z = 0.5$. The k–l based models have similar features to those shown in Fig. 5. In both plots, the relatively cold inlet air can be seen to rapidly fall on entering the room, soon being deflected horizontally by the floor giving rise to a wall jet. Clearly, there is strong streamline curvature (which the cubic model has the ability to model the consequences of) and complex flow physics.

The accuracy of the models tested is summarised in Table 4 which gives the relative error at each of the nine profiles. The errors given in Table 4 and other tables are obtained using the following equation – error (%) $= (|\phi_{\mathrm{CFD}} - \phi_{\mathrm{Exp}}|/|\phi_{\mathrm{Exp}}|) \times 100$. The table shows that overall the k–ϵ based models are more accurate than the k–l by about 5%. This is to be expected. The k–ϵ model is more complete having more plausible local dissipation levels. The l equations in the k–l model will be inadequate near the inlet jet region. Also, they certainly have insufficient physics to deal with the complex wall jet flow near the floor. Numerous other complex flow features are also present which will challenge the relatively simplistic turbulence length scale equations used in Wolfshtein's standard k–l model. Considering this, the 5% accuracy loss for the k–l model seems relatively small.

The relatively high errors reported in Table 4 can partly be explained by measurement errors. The hot-sphere anemometers errors are of significant importance at low velocities ($\simeq$0.1 m/s). The table shows that the EASM k–ϵ is most accurate. The accuracy improvements found using the EASM and cubic model over the linear k–ϵ model are however much less (<1%) than seen for simpler validation and room geometry cases. In a k–l framework, the EASM has the same overall accuracy as the linear model and, the cubic the worst accuracy of all the models. The cubic model's poor k–l accuracy can be partly attributed to the Wolfshtein near wall damping function(s) being inappropriate for the model – some re-calibration being necessary.

Fig. 6 compares temperature measurements for four profiles (at $X = Z = 0.5$; $X = 0.166$, $Z = 0.5$; $X = 0.5$,

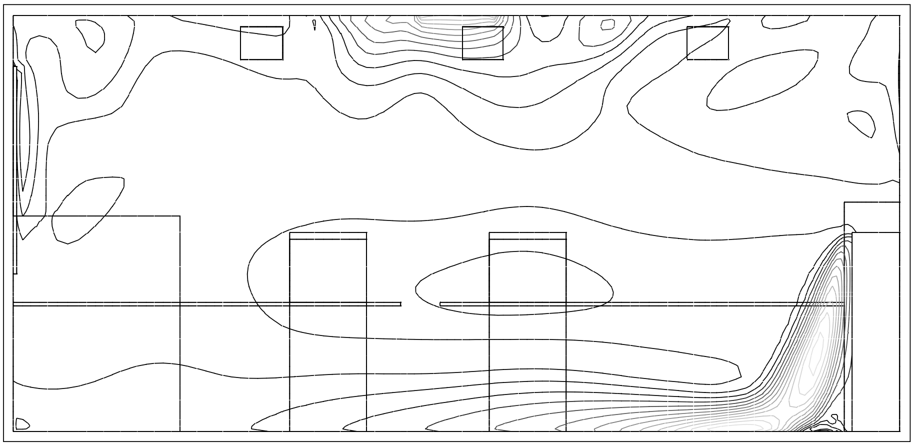
(a)

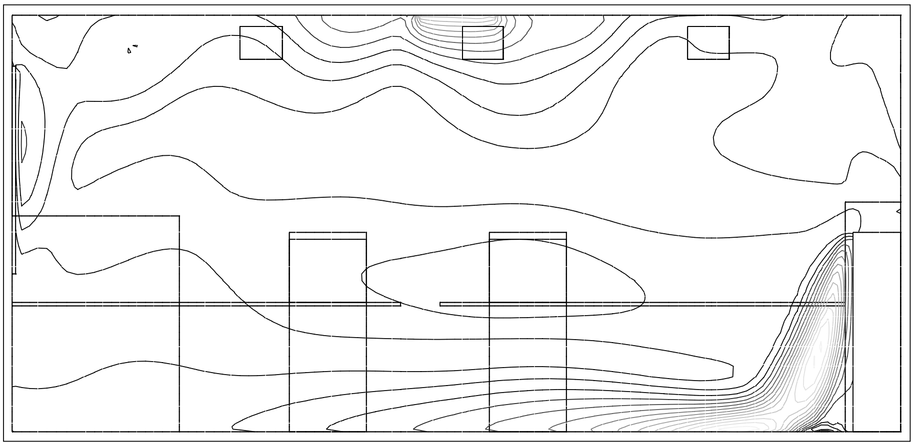
(b)

Fig. 5. Velocity contour plots in the room for (a) the linear and (b) EASM k–ϵ models.

Table 4
Relative velocity error for each of the nine measured profiles

Profile	*k–l*			*k–ε*		
	Linear	EASM	Cubic	Linear	EASM	Cubic
1	90.3	49.5	98.5	51.5	53.3	42.9
2	67.0	57.9	98.1	59.1	48.0	59.6
3	43.7	16.8	41.4	26.8	22.3	25.0
4	41.2	47.2	38.6	32.9	25.4	30.7
5	34.2	55.3	52.5	59.1	53.5	61.9
6	25.4	37.6	18.5	25.1	23.4	25.9
7	35.3	54.8	50.5	46.7	56.7	50.1
8	23.4	65.6	31.4	26.1	36.9	32.2
9	36.2	12.6	23.7	23.1	21.7	21.2
Average	44.1	44.1	50.4	38.9	37.9	38.8

$Z = 0.166$ and $X = 0.5$, $Z = 0.66$) with the linear, EASM and cubic k–ϵ model predictions. Fig. 7 is a repeat of Fig. 6 using this time k–l based models. Fig. 7 shows that, unlike the k–ϵ, all k–l based models are unable to predict the correct thermal stratification in the lower part of the room ($Y < 0.4$).

Table 5 gives a summary of temperature prediction errors for all profiles and models. The table shows that, as for the velocities, the k–l based models give greater errors than the k–ϵ based models ($\simeq$2%). Moreover, the EASM and cubic k–l models have a higher error than the linear k–l model. Again, this worse nonlinear model performance could be attributed to the inappropriateness of the standard k–l model's near wall modelling. The EASM k–l model now gives the biggest overall error. In a k–ϵ framework, the EASM and cubic models are found to very marginally improve linear model accuracy. For this case, buoyancy plays a key role. The modelling of turbulence production by buoyancy, and the general turbulent heat fluxes, is relatively crude making use of the simple eddy-diffusivity approximation. This crude modelling element might well negate the benefits of using the additional nonlinear terms. This could explain the similarity between the linear and nonlinear model results.

5.2. Jouvray (J1 and J2) cases

Finally comparison is made with the Jouvray data with its carefully controlled boundary conditions.

5.2.1. Thermal stratification

Fig. 8 compares the averaged measured and predicted vertical thermal stratification in the room for cases J1 (Frame (a)) and J2 (Frame (b)). The wall temperatures are averages over all walls at a particular height. The fluid temperatures are local values at the centre of the room. Since it has best overall accuracy, the EASM k–ϵ is chosen for the comparison. Temperature is normalized by the inlet temperature and height by the room's height. In Frame (a), the EASM k–ϵ (a) result uses averaged wall temperature boundary conditions and the EASM k–ϵ (b) result uses the polynomial T_s fit. As can be seen from the figure, only minor differences are observed between the two boundary

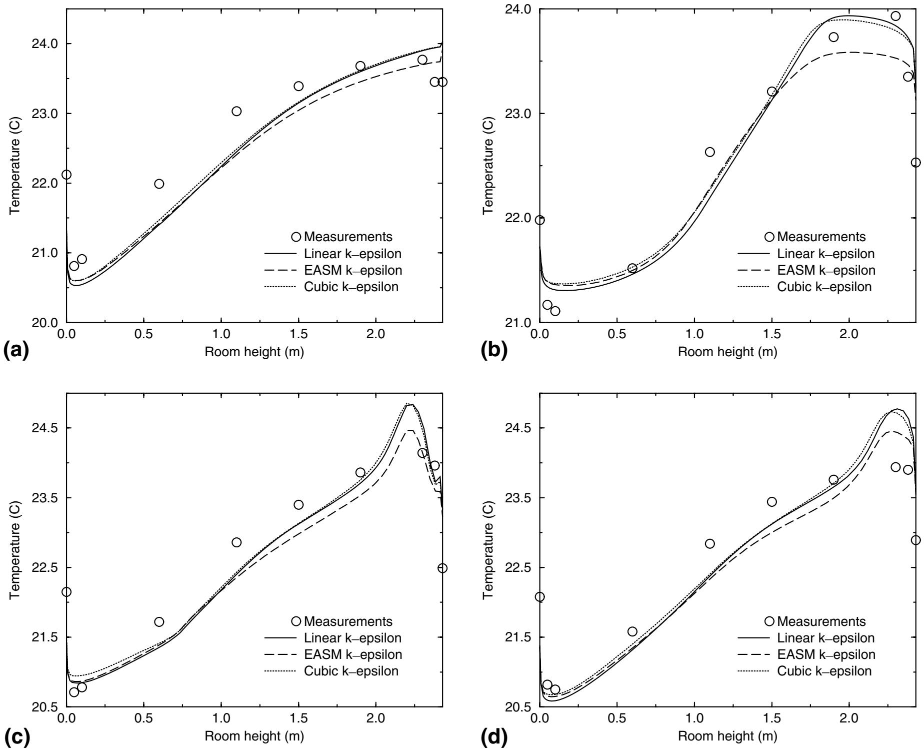

Fig. 6. Comparison of measured temperature profiles with predictions of the linear, EASM and cubic k–ϵ models at the following locations: (a) $X = Z = 0.5$; (b) $X = 0.166$, $Z = 0.5$; (c) $X = 0.5$, $Z = 0.166$ and (d) $X = 0.5$, $Z = 0.66$.

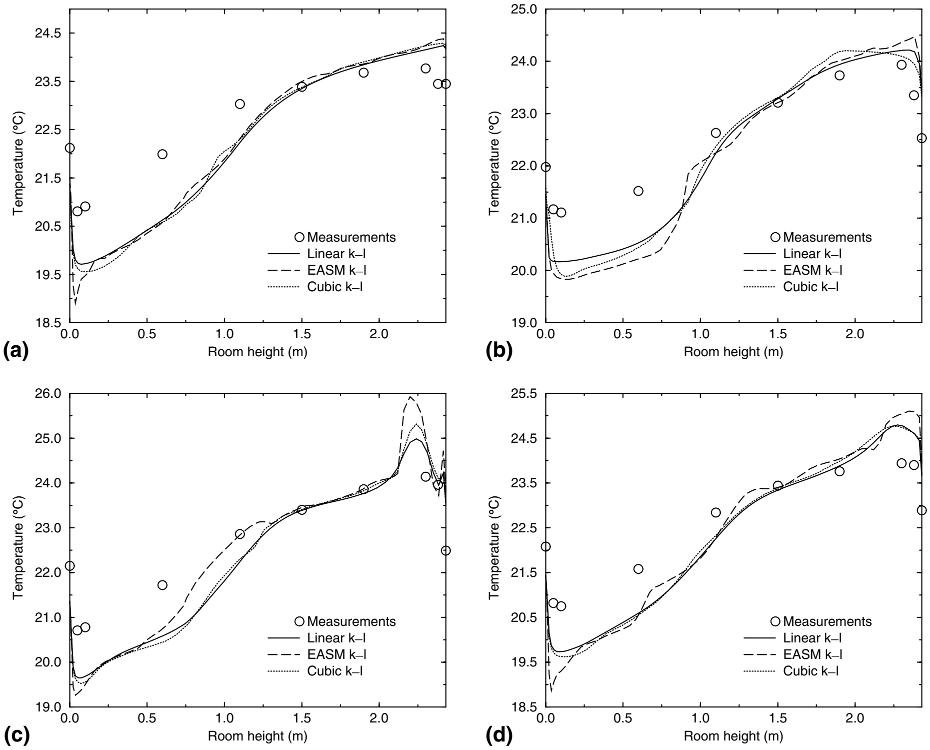

Fig. 7. Comparison of measured temperature profiles with predictions of the linear, EASM and cubic *k–l* models at the following locations: (a) $X = Z = 0.5$; (b) $X = 0.166$, $Z = 0.5$; (c) $X = 0.5$, $Z = 0.166$ and (d) $X = 0.5$, $Z = 0.66$.

Table 5
Relative temperature error for each of the nine measured profiles

Profile	*k–l*			*k–ϵ*		
	Linear	EASM	Cubic	Linear	EASM	Cubic
1	4.16	4.76	3.98	3.22	2.94	3.25
2	2.95	3.60	3.10	1.70	1.50	1.61
3	3.10	3.45	3.38	1.88	1.80	1.76
4	2.20	3.32	2.37	0.97	1.11	0.89
5	2.48	3.02	2.40	0.90	0.89	0.91
6	2.51	2.62	2.79	1.37	1.46	1.36
7	2.62	3.63	2.97	1.58	1.82	1.50
8	2.61	3.39	2.74	1.67	1.47	1.47
9	2.74	3.57	2.74	1.43	1.51	1.32
Average	2.82	3.48	2.94	1.64	1.61	1.56

conditions. The other flow variables are also found to be insensitive to the changes in boundary conditions. Hence, for simplicity, the results presented thereafter use average wall temperature boundary conditions. Frame (a) shows that, like the case of Yuan et al. (1999), the magnitude of the thermal stratification is not well predicted especially in the vicinity of the floor and ceiling. The figure also shows that the average surface temperature is of lower magnitude than the airflow temperature. Similar temperature magnitudes are found away from the floor and ceiling. As noted earlier, the relatively poor agreement in the near wall region can perhaps be partly explained by the use of simple models for heat transfer and buoyancy effects. The use of more advanced models is left as future work.

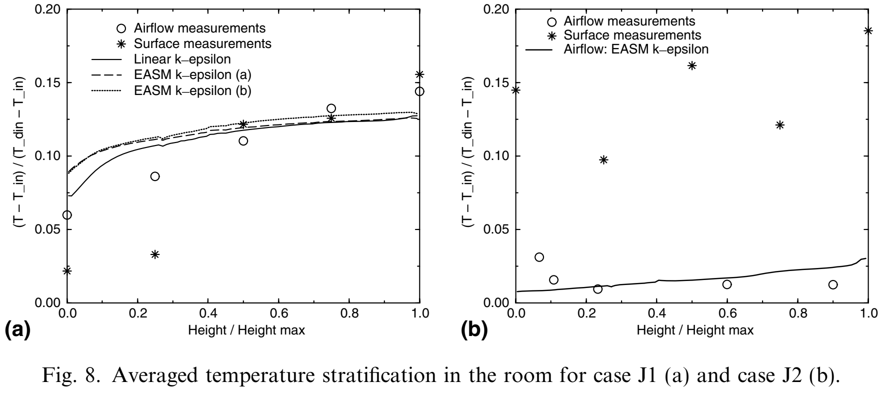

Fig. 8. Averaged temperature stratification in the room for case J1 (a) and case J2 (b).

Table 6
Averaged temperature error (%) of the models for cases J1 and J2

Case	Linear		EASM		Cubic	
	k–l	k–ϵ	k–l	k–ϵ	k–l	k–ϵ
Case J1	8.5	8.4	3.9	3.7	3.8	3.4
Case J2	7.1	6.8	6.8	6.3	7.0	6.6

In Frame (b) of Fig. 8, the EASM k–ϵ model predictions are compared with the averaged measurements of wall and air temperature. Unlike for case J1, this plot shows, as might be expected, that a clear thermal stratification is no longer present. Away from the floor region (top 80% of the room) the predictions of the EASM k–ϵ model are found to agree reasonably well with air temperature measurements. The figure also indicates that the averaged surface temperatures (used as boundary conditions) are higher than the air temperatures.

The temperature prediction accuracies of the RANS models are summarised in Table 6. The table shows that, for displacement ventilation Case J1, the use of the EASM and cubic models significantly improves linear model accuracy. This is in strong contrast to the displacement ventilation Case Y1 where the linear and nonlinear results are similar. For case J2, the improvements found using the EASM or cubic models are minor. The EASM, in either the k–l or k–ϵ frameworks has marginally best accuracy.

5.2.2. Air velocities

Fig. 9 plots measured against predicted room velocities for cases J1 and J2. For perfect agreement the symbols would lay on the 45° line. The dashed lines effectively represent measurement error bars. It is clear from both figures that the highest velocities in the room (in the vicinity of the idealized occupant) are not well predicted for any of the models. The highest velocity measurement in the room is produced by a top opening of the idealized occupant. In contradiction to the measurements, the models tested all predict that the probe measuring this highest velocity is located outside of the high velocity convective area of the idealized occupant. Further investigation on the boundary conditions applied to the top area of the idealized occupant is required to make any significant conclusions. This is left as future work. The convective area of the idealized occupant as well as the overall airflow patterns in the room are illustrated by the velocity contour plots for cases J1 and J2 in Fig. 10. Frame (a) gives the linear k–ϵ model contours for Case J1. Frames (b) and (c) gives linear and EASM k–ϵ results for Case J2. In all plots the convective plume around the idealized occupant is clear. This seems to give rise to a wall jet like boundary layer on the upper horizontal surface (ceiling). In Frames (b) and (c) for case J2, the linear and nonlinear RANS results show significant qualitative flow differences. There perhaps seems greater similarity between the linear k–ϵ velocity contour plots for the different J1 and J2 cases shown in frames (a) and (b).

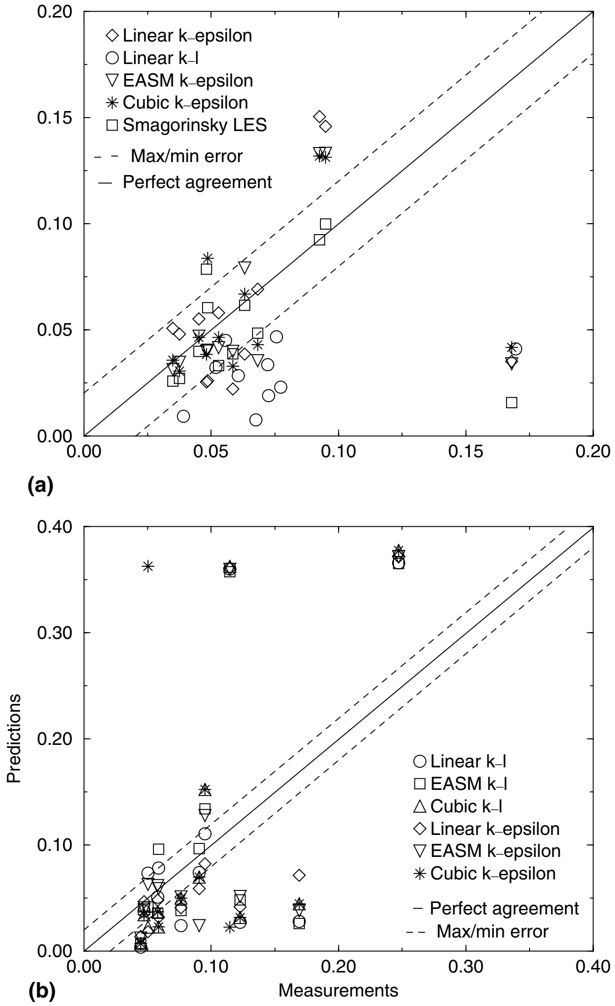

Fig. 9. Comparison of measured and predicted airflow velocities for case J1 (a) and case J2 (b).

To emphasize the differences between the models tested, the averaged velocity errors for cases J1 and J2 are presented in Table 7. The table shows that, once more, the less complete k–l based models have significantly lower accuracy than the k–ϵ based, especially for case J1. The relatively low velocity predictive accuracy seen in Table 7 is partly explained by the low measurement accuracy for velocities (±0.02 m/s). It can, however, be noted that these prediction errors are of lower magnitude than previously seen for the Y1 case. This could be because the measurements being compared with have more carefully defined boundary conditions.

For Case J2 the linear and nonlinear models give similar velocity results. For Case J1, relative to the linear equivalent, both cubic and EASM models are found to substantially improve accuracy. The EASM k–ϵ model is only 0.5% less accurate than the LES. The latter, besides having best agreement with measurements, is extremely computationally expensive compared to the EASM. The cubic model is not always found to improve accuracy. The LNS model results are encouraging. However, this could

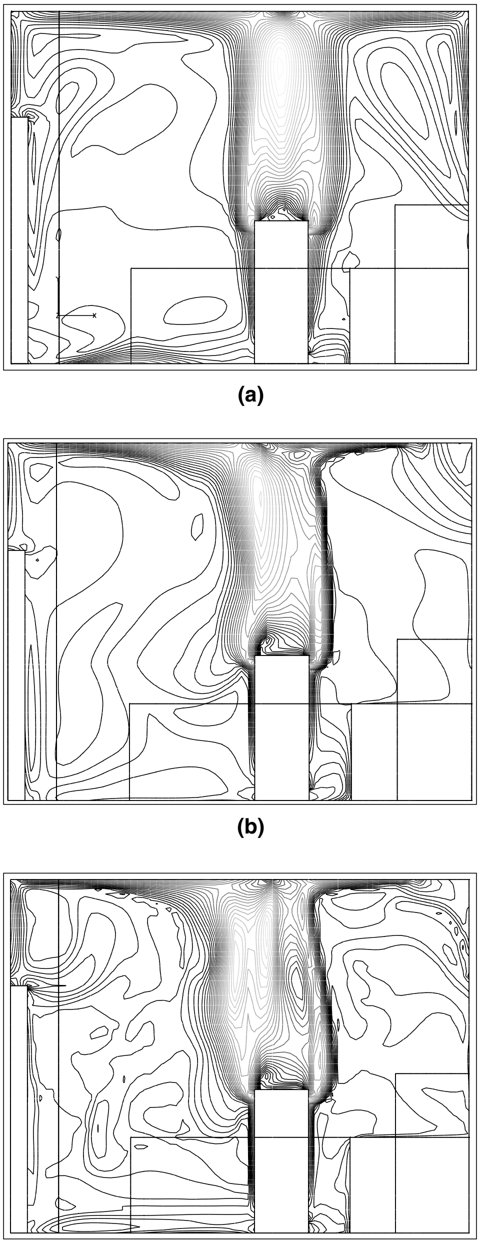

Fig. 10. Velocity contour plots in the idealized occupants mid-plane for: (a) linear k–ϵ model, Case J1; (b) linear k–ϵ model, Case J2 and (c) EASM k–ϵ model, Case J2.

Table 7
Averaged velocity errors (%)

	Linear		EASM		Cubic		LES	LNS
	k–l	*k–ϵ*	*k–l*	*k–ϵ*	*k–l*	*k–ϵ*		
Case J1	58.5	34.7	47.3	22.2	50.0	24.6	21.7	23
Case J2	26.9	25.9	26.3	24.3	30.1	28.1	N/A	N/A

be fortuitous. LNS is quite capable of producing RANS zones which are upstream of LES zones. This situation will give rise to inappropriate upstream LES boundary conditions. This LNS defect can be remedied using a relatively complex to implement synthetic turbulence generation procedure.

5.2.3. Gas tracer decay

Fig. 11 compares the measured and EASM predicted scalar decay in the breathing zone of the room ($Y = 0.533$) for cases J1 and J2. Both figures are non-dimensionalised by the time required to renew the air in the room and by the target gas tracer concentration of 10 ppm. For both cases, reasonable agreement is found between measurements and predictions. The relative scalar decay prediction errors for the models used are summarised in Table 8. The table shows that even for this global parameter again (for reasons outlined earlier) the *k–l* based models have lower accuracy than the k–ϵ. The overall predicted gas tracer accuracy of case J2 is better than for case J1. The EASM, in either the *k–l* or the k–ϵ framework, is found to give the best decay predictions. In particular, close agreement is found using the EASM for case J2 (<6% relative error). The accuracy improvements found using the cubic model are lower than those of the EASM.

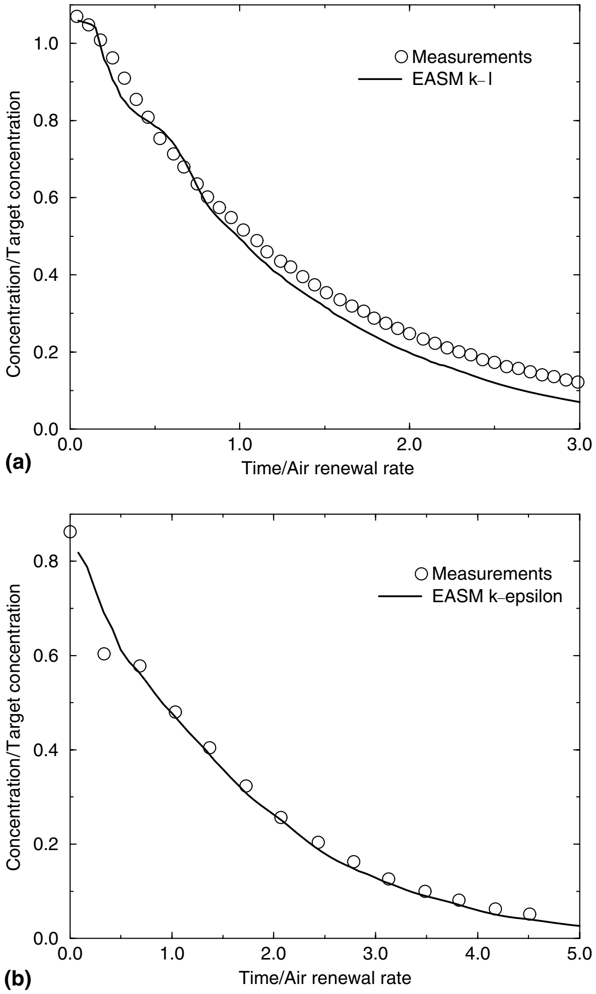

Fig. 11. Averaged concentration decay for: (a) case J1 and (b) case J2.

Table 8
Relative averaged scalar decay error (%) of the models compared with measurements

Case	Linear		EASM		Cubic	
	k–l	k–ϵ	k–l	k–ϵ	k–l	k–ϵ
Case J1	22.4	19.2	17.7	17.2	21.4	18.5
Case J2	13.4	10.9	9.7	9.1	11.5	10.5

Table 9
Contaminant removal index

	Measurement	Linear		EASM		Cubic	
		k–l	k–ϵ	k–l	k–ϵ	k–l	k–ϵ
Case J1	1.0	1.05	0.97	1.02	0.98	1.09	1.05
Case J2	1.09	1.14	1.11	1.11	1.10	1.17	1.07

Ventilation efficiency is assessed using the contaminant removal index E_f. Following Collignan and Riberon (2000), this is defined as $E_f = C_{ra}/C_{ws}$, where C_{ra} is the concentration at the room's flow outlet and C_{ws} the concentration in the breathing zone. In simulations, the tracer gas is supplied at time $t = 0$ only. Table 9 summarizes the predicted E_f for the various models tested. The table shows that the k–ϵ based models have higher accuracy than the k–l based models. The table also shows that for cases J1 and J2, the cubic model in a k–l framework has worse accuracy than its linear equivalent. Again the EASM models are found to be most accurate.

Our group has contrasted these cubic and EASM models for a much wider range of relatively low Reynolds number flows than explored here (see, for example, Tucker et al. (2003)). This work suggests that the performance of the cubic model relative to the EASM is strongly case dependent. Hence, it is difficult to draw firm conclusions of the relative merits of the EASM and cubic models.

6. Conclusions

As would be expected, the k–l based predictions (for which l equations are case dependent) have a lower accuracy than the k–ϵ. It is important to note that the former type of model, with its algebraic turbulence length scale description, is most popular in room ventilation modelling. Overall, the EASM k–ϵ is found to give marginally better agreement with measurements, in terms of velocities, temperatures and passive scalar decay. For case J1, the EASM k–ϵ is found to predict velocities within 0.5% of the Smagorinsky LES. The latter is, as would be expected, substantially more computationally demanding than any of the RANS models. The LNS simulation gives encouraging case J1 velocity predictions. However, this result could be fortuitous. For complex flows LNS can give rise to LES zones with inappropriate upstream RANS boundary conditions. The cubic is found to give slightly more mixed results than the EASM. It improves temperature and passive scalar decay predictions but gives worse case J2 velocities than its linear equivalent. For the case J1 displacement ventilation study, poor RANS thermal stratification predictions are found. This can perhaps partly be explained by the simplicity of the heat transfer and buoyancy models used.

Where comparison with measurements is made, LES gives the best accuracy. The cubic model is found to be more unstable than the EASM. However, for other cases not reported here the stability and accuracy traits of the cubic in relation to the EASM are reversed. Hence, many of the performance aspects discussed seem highly case dependent.

Appendix A. Supplementary data

Supplementary data associated with this article can be found, in the online version, at doi:10.1016/j.ijheatfluidflow.2006.02.029.

References

Abe, K., Kondoh, T., Nagano, Y., 1996. A new turbulence model for predicting fluid flow and heat transfer in separating and reattaching flows, thermal field calculations. Int. J. Heat Mass Transfer 38 (8), 1467–1481.

Batten, P., Goldberg, U., Chakravarthy, S., 2002. LNS – An approach towards embedded LES. AIAA paper, AIAA-2002-0427.

Chen, Q., 1996. Comparison of different k–ϵ models for indoor airflow computations. Numer. Heat Transfer, Part B: Fundam. 28, 353–359.

Chen, Q., 1997. Computational fluid dynamics for HVAC: successes and failures. ASHRAE Trans. 103, 178–187.

Chen, Q., Xu, W., 1998. A zero-equation turbulence model for indoor airflow simulation. Energy Build. 28, 137–144.

Chikamoto, T., Murakami, S., Kato, S., 1992. Numerical simulation of velocity and temperature fields within atrium based on modified k–ϵ model incorporating damping effect due to thermal stratification. In: Proc. ISRACVE, Tokyo.

Collignan, C., Riberon, J., 2000. A numerical study on polutant removal effectiveness of a room. In: Awbi, H.B. (Ed.), Proc. Roomvent II. Elsevier Science Ltd, Amsterdam, pp. 931–936.

Craft, T.J., Launder, B.E., Suga, K., 1996. Development and application of a cubic eddy viscosity model of turbulence. Int. J. Heat Fluid Flow 17, 108–115.

Craft, T.J., Iacovides, H., Yoon, J.H., 1999. Progress in the use of non-linear two-equation models in the computation of convective heat-transfer in impinging and separated flows. Flow Turbul. Combust. 63, 59–80.

Davidson, L., 2001. A hybrid LES–RANS model based on a one-equation SGS model and a two-equation k–ω model. In: Proc. 2nd Int. Symp. on Turbulence and Shear Flow Phenomena 2 (Stockholm). pp. 175–180.

Davidson, L., Nielsen, P.V., 1996. Large eddy simulations of the flow in a three-dimensional ventilated room. In: Proc. Roomvent 2. pp. 161–168.

Davidson, L., Nielsen, P.V., Topp, C., 2000. Low-Reynolds number effect in ventilated rooms: a numerical study. In: Awbi, H.B. (Ed.), Proc. Roomvent I. Elsevier Science Ltd, Amsterdam, pp. 307–312.

Emmerich, S.J., McGrattan, K.B., 1998. Application of a large eddy simulation model to study room airflow. ASHRAE Trans., Part 1-B 104, 1128–1140.

Gatski, T.B., Speziale, C.G., 1993. On explicit algebraic stress model for complex turbulent flows. J. Fluid Mech. 254, 59–78.

Jacobsen, T.V., Nielsen, P.V., 1993. Numerical modelling of thermal environment in a displacement-ventilated room. In: Proc. Indoor Air, vol. 5. pp. 301–306.

Jouvray, A., 2003. Computation and measurements of flows in rooms. Ph.D. Thesis, School of Engineering, University of Warwick, UK.

Kim, T., Kato, S., Murakami, S., 2001. Indoor cooling/heating load analysis based on coupled simulation of convection, radiation and HVAC control. Build. Environ. 36, 901–908.

Lam, C.K.G., Bremhorst, K., 1981. A modified form of the k–ϵ model for predicting wall turbulence. ASME J. Fluid Eng. 103, 456–460.

Launder, B.E., Spalding, D.B., 1974. The numerical computation of turbulent flows. Comput. Meth. Appl. Mech. Eng. 3, 269–289.

Lin, Z., Chow, T.T., Fong, K.F., Chen, Q., 1999. Validation of CFD model for research into application of displacement ventilation to Hong Kong buildings. In: Proc. 3rd Int. Symp. on HVAC II (Shenzhen, China). pp. 602–613.

Müller, D., Davidson, L., 2000. Comparison of different subgrid turbulence models and boundary conditions for large-eddy-simulation of room air flows. In: Awbi, H.B. (Ed.), Proc. Roomvent I. Elsevier Science Ltd, Amsterdam, pp. 301–306.

Nielsen, P.V., Restivo, A., Whitelaw, J.H., 1978. The velocity characteristics of ventilated rooms. J. Fluid Eng. 100, 291–298.

Patankar, S.V., Spalding, D.B., 1972. A calculation procedure for heat mass and momentum transfer in three dimensional parabolic flows. Int. J. Heat Mass Transfer 15, 1787–1806.

Peng, S.H., 1998. Modelling of turbulent flow and heat transfer for building ventilation. Ph.D. Thesis, Chalmers University of technology, Gothenburg, Sweden.

Peng, S.H., Davidson, L., 2000. The potential of large eddy simulation techniques for modelling indoor air flows. In: Awbi, H.B. (Ed.), Proc. Roomvent I. Elsevier Science Ltd, Amsterdam, pp. 295–300.

Peng, S.H., Davidson, L., Holmberg, S., 1996. Performance of two-equation turbulence models for numerical simulation of ventilated rooms. In: Proc. Roomvent 2. pp. 153–160.

Peng, S.H., Davidson, L., Holmberg, S., 1997. A modified low Reynolds number k–ω model for recirculating flows. ASME J. Fluid Eng. 119, 867–875.

Rodi, W., 1975. The prediction of free turbulent boundary layers by the use of a two-equation model of turbulence. Ph.D. Thesis, University of London, UK.

Rodi, W., Mansour, N.N., Michelassi, V., 1993. One equation near wall turbulence modelling with the aid of direct simulation data. J. Fluid Eng. 115, 196–205.

Shaw, C.Y., 2000. Evaluating seven diffuser layouts: ventilation for Workstations. ASHRAE J., 52–59.

Sinai, Y.L., Owens, M.P., McLaughlin, A., 2000. Case study: CFD modelling of HVAC in the Greenwich millennium dome. In: Awbi, H.B. (Ed.), Proc. Roomvent II. Elsevier Science Ltd, Amsterdam, pp. 1165–1170.

Smagorinsky, J., 1963. General circulation experiments with the primitive equations. I. The basic experiment. Monthly Weather Rev. 91 (3), 99–164.

Speziale, C.G., 1998. Turbulence modeling for time-dependent RANS and VLES: a review. AIAA J. 36 (2), 173–184.

Tucker, P.G., 2001. Computation of unsteady internal flows. Kluwer Academic Publishers, Dordrecht.

Tucker, P.G., Davidson, L., 2004. Zonal k–l based large eddy simulations. Comput. Fluids 33, 267–287.

Tucker, P.G., Liu, Y., Chung, Y.M., Jouvray, A., 2003. Computation of an unsteady complex geometry flow using novel non-linear turbulence models. Int. J. Numer. Meth. Fluids 43 (9), 979–1001.

Wolfshtein, M., 1969. The velocity and temperature distribution in one-dimensional flow with turbulence augmentation and pressure gradient. Int. J. Heat Mass Transfer 12, 301–318.

Xu, W., Chen, Q., 2001a. A two-layer turbulence model for simulating indoor airflow; Part I. Model development. Energy Build. 33, 613–625.

Xu, W., Chen, Q., 2001b. A two-layer turbulence model for simulating indoor airflow; Part II. Applications. Energy Build. 33, 627–639.

Yakhot, V., Orzag, S.A., Thangam, S., Gatski, T.B., Speziale, C.G., 1992. Development of turbulence models for shear flow by a double expansion techniques. Phys. Fluids A 4 (7), 1510.

Yap, C.R., 1987. Turbulent heat and momentum transfer in reciculating impinging flows. Ph.D. Thesis, Faculty of Technology, University of Manchester.

Yoon, J., Lee, K., Lee, J., 2000. Computer simulation of the indoor environments with cooling and heating systems: the great hall in the Inchon international airport terminal. In: Awbi, H.B. (Ed.), Proc. Roomvent II. Elsevier Science Ltd, Amsterdam, pp. 1195–1200.

Yuan, X., Chen, Q., Glicksman, L.R., Hu, Y., Yang, X., 1999. Measurements and computations of room airflow with displacement ventilation. ASHRAE Trans. 105, 340–352.